LiNbO₃ and AlGaAs On-Insulator Platforms for Second Harmonic Generation: Comparison and Perspectives.

Jack Haines,* Pooja Uday Naik, and Massimiliano Guasoni Optoelectronics Research Centre, University of Southampton, Southampton SO17 1BJ, UK.

Marco Gandolfi

Dipartimento di Ingegneria dell'Informazione, Università degli Studi di Brescia, Via Branze 38, 251238 Brescia, Italy Consiglio Nazionale delle Ricerche - Istituto Nazionale di Ottica, Via Branze 45, 25123 Brescia, Italy and Consorzio Nazionale Interuniversitario per le Telecomunicazioni (CNIT),

Viale G.P. Usberti 181/A Sede11 Scientifica di Ingegneria-Palazzina 3, 43124 Parma, Italy

(Dated: April 23, 2025)

The rise of aluminium gallium arsenide on insulator (AlGaAsOI) and lithium niobate on insulator (LNOI) platforms presents new opportunities for advancing on-chip and ultra-compact nonlinear photonic devices. In this study, we investigate theoretically and via numerical simulations second harmonic generation (SHG) in AlGaAsOI and LNOI waveguides across a wide range of pulse widths, from the sub-picosecond to the continuous wave regime, and peak power levels spanning from milliwatt to hundreds of watts. Our research aims to identify optimal time and power regimes for achieving high SHG conversion efficiency, exploring the detrimental impact of linear and nonlinear losses as well as dispersion effects. Additionally, we assess the performance of SHG against manufacturing errors and surface roughness, comparing our findings with state-of-the-art solutions. These results offer insights into the robustness and potential applications of SHG in these advanced photonic platforms.

I. INTRODUCTION

The recent development of aluminium gallium arsenide on insulator (AlGaAsOI) [1, 2] and lithium niobate on insulator (LNOI) [3, 4] platforms is challenging the status quo of silicon photonics in integrated optics. These platforms merge the benefits of the traditional counterparts grown on their native substrate, namely a large nonlinear response and low two-photon absorption (TPA), along with the strong field confinement originating from the low-index cladding. This, in turn, further boosts the nonlinearity and opens up new perspectives in nonlinear photonics. A key application is the development of a novel class of waveguides for nonlinear wavelength conversion with an efficiency comparable or even superior to that found in conventional nonlinear platforms like crystals, periodically poled lithium niobate (PPLN) waveguides and AlGaAs/GaAs waveguides [5–16], whilst offering at the same time on-chip integration and far greater compactness. In the last few years, several works have reported on nonlinear wavelength conversion in LNOI [17–20] and AlGaAsOI [21–28] waveguides and nanostructures. However, at present there is a lack of general overview regarding the conversion efficiency and the level of miniaturization that can be achieved in different regimes of pump power and pulse duration.

In this work, we analyse theoretically and via numerical simulations the nonlinear dynamics of AlGaAsOI and LNOI waveguides from the sub-picosecond to the contin-

uous wave regime and for different power levels, identifying the most suitable conditions to achieve high conversion efficiency and comparing the performance against state-of-the-art solutions. We investigate second harmonic generation (SHG), a crucial process for nonlinear conversion that can be extremely efficient in LNOI and AlGaAsOI waveguides. We focus on a scenario that simplifies the fabrication of the device and the experimental setup as much as possible and enhances the robustness of manufacturing errors. Firstly, we consider rectangular waveguides, where the number of parameters to be optimized is minimized (width and height of the crosssection). Second, we assume that the input field at the waveguide is coupled to the fundamental mode, whose excitation is straightforward and typically leads to higher coupling efficiency compared to higher-order modes.

This paper is organized as follows. In section 2 we present the set of coupled differential equations describing the spatio-temporal dynamics of light propagation in the waveguides under analysis and introduce some optimal configurations for efficient SHG in LNOI and AlGaAsOI waveguides. In section 3 we introduce the effective lengths of the different physical effects at play and in section 4 we discuss the maximum conversion efficiency (CE) achievable in each configuration as a function of pump power and pulse width. In section 5 we outline the robustness of the nonlinear conversion with respect to manufacturing errors as well as surface roughness. Finally, in Section 6, we conclude by comparing our findings against recent state-of-the-art solutions for SHG.

^{*} Optoelectronics Research Centre, University of Southampton, Southampton SO17 1BJ, UK.; j.m.haines@soton.ac.uk

II. NUMERICAL MODELLING AND PARAMETERS

We consider rectangular LiN and $Al_{0.25}Ga_{0.75}As$ waveguides embedded in a low refractive index insulator cladding (see Fig.1), which is typically silicon dioxide (SiO₂) or hydrogen silsesquioxane (HSQ). The latter has a refractive index similar to the index of SiO₂ [21], therefore the results discussed in this work are almost identical whether SiO₂ or HSQ are used.

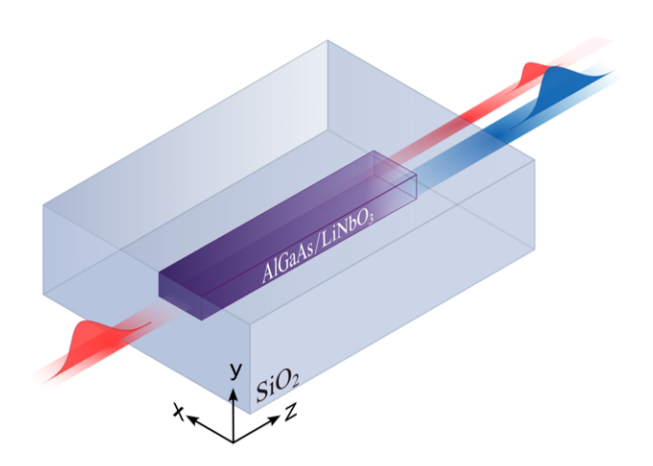


FIG. 1. Schematic of the system under investigation made of a waveguide with AlGaAs or LiN core and surrounded by SiO_2 . The input beam at the fundamental frequency (red) from the left is converted to a second harmonic frequency beam (blue) on output.

A pump beam at the fundamental frequency (FF) ω_f is launched into the waveguide coupled to the spatial mode \mathbf{m}_f and generates light at the second harmonic (SH) $\omega_s = 2\omega_f$ into the mode \mathbf{m}_s via nonlinear conversion. In this work, we focus on the standard case of near-IR to near-visible conversion where the FF and SH wavelengths are respectively $\lambda_f = 2\pi c/\omega_f = 1550$ nm and $\lambda_s = 2\pi c/\omega_s = 775$ nm (c is the speed of light in the vacuum). The following system of coupled equations describes the spatio-temporal evolution of the FF and SH envelopes $A_f(\mathbf{z},\mathbf{t})$ and $A_s(\mathbf{z},\mathbf{t})$ [29–31], respectively:

$$\frac{\partial A_s}{\partial z} + \Delta \beta_1 \frac{\partial A_s}{\partial t} + \frac{i}{2} \beta_{2s} \frac{\partial^2 A_s}{\partial t^2} = -\frac{\alpha_s}{2} A_s + i p A_f^2 e^{-i\Delta \beta z} + i \gamma_s A_s (R_{ss} |A_s|^2 + 2R_{sf} |A_f|^2)$$

$$(1)$$

$$\frac{\partial A_f}{\partial z} + \frac{i}{2}\beta_{2f}\frac{\partial^2 A_f}{\partial t^2} = -\frac{\alpha_f}{2}A_f + ipA_sA_f^*e^{i\Delta\beta z} + i\gamma_f A_f (R_{ff}|A_f|^2 + 2R_{fs}|A_s|^2)$$
(2)

 β_{2n} and α_n indicate respectively the group velocity dispersion (GVD) and the linear losses at the frequency ω_n , $n=\{f,s\}$, whereas $\Delta\beta_1$ is the differential inverse group velocity (DIGV) between the SH mode and the FF mode. The SHG coefficient is $p=\sqrt{2}\omega_s\epsilon_0\Phi_{NL}$, where ϵ_0 is the vacuum permittivity and Φ_{NL} reads [29]:

$$\begin{split} \Phi_{NL}(LiN,X-cut) &= \\ d_{22} \int_{\text{Core}} m_{fx}^2 m_{sz}^* - m_{fy}^2 m_{sz}^* \\ &- 2 m_{fy} m_{fx} m_{sy}^* \ dx dy \\ + d_{31} \int_{\text{Core}} 2 m_{fx} (m_{fy} m_{sy}^* + m_{fz} m_{sz}^*) \\ &+ m_{fy}^2 m_{sx}^* + m_{fz}^2 m_{sx}^* \ dx dy \\ + d_{33} \int_{\text{Core}} m_{fx}^2 m_{sx} \ dx dy \end{split}$$

$$\Phi_{NL}(AlGaAs) =$$

$$d_{eff} \int_{\text{Core}} 2m_{sx}^* m_{fy} m_{fz} + 2m_{sy}^* m_{fx} m_{fz}$$

$$+ 2m_{sz}^* m_{fy} m_{fx} dx dy$$
(4)

 $\Phi_{NL}({\rm LiN~Z-cut})$ is found from $\Phi_{NL}({\rm LiN~X-cut})$ by replacing $m_{nx} \to m_{ny}, \ m_{ny} \to m_{nz}, \ m_{nz} \to m_{nx}$, where m_{nx}, m_{ny}, m_{nz} are the x,y and z electric field components of the spatial mode ${\bf m}_n$, and the spatial modes are normalised so that $|A_f(z,t)|^2$ and $|A_s(z,t)|^2$ represent the FF and SH power.

The Kerr nonlinear coefficient $\gamma_n = n_{2,n} \omega_n/c + i\beta_{tpa,n}/2$, where $n_{2,n}$ and $\beta_{tpa,n}$ are respectively the nonlinear refractive index and the TPA coefficient at frequency ω_n . Note that the last two terms on the right-hand side of Eqs.(1,2) account respectively for self-phase modulation (SPM) and cross-phase modulation (XPM). In the case of rectangular waveguides, where modes are mainly linearly polarized along one of the axes, the cubic overlap coefficients R_{nq} (n={f, s},q={f, s}) can be approximated as follows:

$$R_{nq} = \frac{\int_{Core} |\mathbf{m}_n|^2 |\mathbf{m}_q|^2 dx dy}{\int_{Core} |\mathbf{m}_n|^2 dx dy \int_{Core} |\mathbf{m}_q|^2 dx dy}$$
(5)

We consider the case where the pump beam is coupled into the fundamental spatial mode TE00, which as previously mentioned represents the most suitable configuration to maximise the coupling efficiency and minimize the complexity of the experimental setup. On the other hand, the SH field may be generated in a higher-order mode. The coefficients $\Delta \beta_1$, β_{2n} , Φ_{NL} and R_{nq} -reported in Table I - are mode dependent and are computed using finite element method software (Comsol Multiphysics),

Conf	\mathbf{m}_f	\mathbf{m}_s	dim	Φ_{NL}	Δeta_1	β_{2f}	$eta_{2 \ m s}$	$ m R_{ff}$	R_{ss}	$R_{\rm sf}$
			(nm^2)	$(A^{-2}W^{1/2})$	$(\mathrm{m}^{-1}\mathrm{ns})$	$(\mathrm{m}^{-1}\mathrm{ps}^2)$	$(\mathrm{m}^{-1}\mathrm{ps}^2)$	$(\mu \mathrm{m}^{-2})$	$(\mu \mathrm{m}^{-2})$	$(\mu \mathrm{m}^{-2})$
LNX	TE00	TE02	960×470	$1.05\mathrm{e}10$	1.0	0.60	0.1	2.0	3.0	1.0
LNZ	TE00	TM02	3945×1162	0.11e10	0	0.05	0.2	0.4	0.5	0.3
AlG	TE00	TM01	575×111	5.20 e10	5.6	10.03	25.0	2.0	0.7	0.7

TABLE I. Parameters and coefficients used in Eqs.(1,2) for the 3 configurations under investigation: conf-LNX is a LiNbO₃ (X-cut) waveguide, conf-LNZ is a LiNbO₃ (Z-cut) waveguide, conf-AlG is a Al_{0.25}Ga_{0.75}As waveguide. Conf = configuration, $\mathbf{m}_f = \mathrm{FF}$ mode, $\mathbf{m}_s = \mathrm{SH}$ mode, dim=transverse dimension (width× height) of the waveguide.

	${ m LiNbO_3}$	AlGaAs
$d_{22} \; (\mathrm{pm/V})$	1.8 [32]	-
$d_{31} \; (\mathrm{pm/V})$	3.7 [33]	-
$d_{33} \; (\mathrm{pm/V})$	20.5 [34]	-
$d_{eff} \; (\mathrm{pm/V})$	-	50 [26, 35 – 37]
$n_2 (\mathrm{m^2/W})$	$1.1 \times 10^{-19} [38, 39]$	$2.0 \times 10^{-17} [40]$
$\beta_{tpaf} \text{ (cm/GW)}$	0 [41]	0.164 [21]

TABLE II. Nonlinear parameters used in Eqs.(1,2).

taking into account the wavelength and refractive index of the materials [42–44]. The nonlinear parameters $d_{22}, d_{31}, d_{33}, d_{eff}, n_{2,n}, \beta_{tpa,n}$ crucially depend on the material properties as well as the wavelength, and partially on the fabrication process itself. Therefore, various studies often report different values for these coefficients at few typical wavelengths. However, our simulations aim to establish general guidelines for conversion efficiency across various regimes of peak power and pulse width. To this end, variations of these coefficients, even up to 100%, do not affect the overall outcomes discussed in the Conclusion section. This stems from the fact that such variations do not alter the order of magnitude of the effective lengths discussed in Section 3.

The nonlinear parameters used in our simulations are detailed in Table II, where we consider $n_{2,f} = n_{2,s} \equiv n_2$ and $\beta_{tpa,f} = \beta_{tpa,s} \equiv \beta_{tpa}$. Note that LiN is practically TPA free for wavelengths beyond 600nm (therefore we set $\beta_{tpa,f} = \beta_{tpa,s} = 0$).

As for linear losses, we analyze 3 different cases that are representative of AlGaAsOI and LNOI waveguides, namely 4 dB/cm, 1 dB/cm and 0.1 dB/cm. While the first two higher losses have become increasingly common [17, 28], the latter instance (0.1 dB/cm) [18] is less common and yet to be achieved in the AlGaAsOI platform. Moreover, for reasons of conciseness, in this work, we assume that losses are equal at the FF and SH. While this is not the general case, as losses are typically frequency dependent, there are nevertheless reported cases where the difference is of the order of ~ 1 dB/cm [17]. In addition, we anticipate significant improvements in the fabrication

processes over the next few years. As a result, it is conceivable that losses as low as $0.1~\mathrm{dB/cm}$ could become the standard in the near future, with differential losses between FF and SH substantially reduced.

The width w and height h of the waveguide are adjusted in order to meet the phase-matching condition for SHG, namely $\Delta \beta = \beta_f(\omega) - \beta_s(2\omega) = 0$, where $\beta_f(\omega)$ is the propagation constant of the FF mode (TE00) and $\beta_s(2\omega)$ is the propagation constant of the SH mode. Table I reports a list of the most suitable phase-matched instances for SHG generation along with the corresponding coefficients used to simulate Eqs.(1,2). The first and third rows (conf-LNX, conf-AlG) represent the configurations that maximize the quadratic nonlinear coefficient p for LNOI (X-cut) and AlGaAsOI waveguides, respectively, whereas the second row (conf-LNZ) corresponds to the case of a null-DIGV between the FF and the SH modes in a LNOI waveguide (Z-cut). Under this condition, the FF and the SH pulses maintain their temporal overlapping as they propagate through the waveguide, which contributes to the build-up of the SH peak power.

Eqs.(1,2) are simulated using input pulses $A_f(z=0,t)$ with Gaussian shape at the FF, whose half width half maximum and peak power are denoted by T_p and P, respectively. The input field is instead null at the SH, namely $A_s(z=0,t)=0$.

A variety of pulse widths T_p are explored in the simulations, ranging from sub-picosecond (100 fs) to nanoseconds, the latter being quasi-continuous waves for the waveguide lengths under investigation. Additionally, the simulations cover a range of peak powers P from sub-Watt (100 mW) up to 100 W. It is worth noting that larger power levels may damage the waveguides.

The main objective of our numerical analysis is the computation of the conversion efficiency (CE) for the 3 configurations of Table I as a function of T_p and P. The CE is defined as:

$$CE = \frac{max\{E_s\}}{E_{in,f}} \tag{6}$$

Here, $\max\{E_s\} = \int_{t=-\infty}^{+\infty} |A_s(z_{max},t)|^2 dt$ is the maximum energy converted at the SH frequency, whereas $E_{in,f} = \int_{t=-\infty}^{+\infty} |A_f(0,t)|^2 dt$ is the total input energy at the FF. The position z_{max} is the longitudinal position in

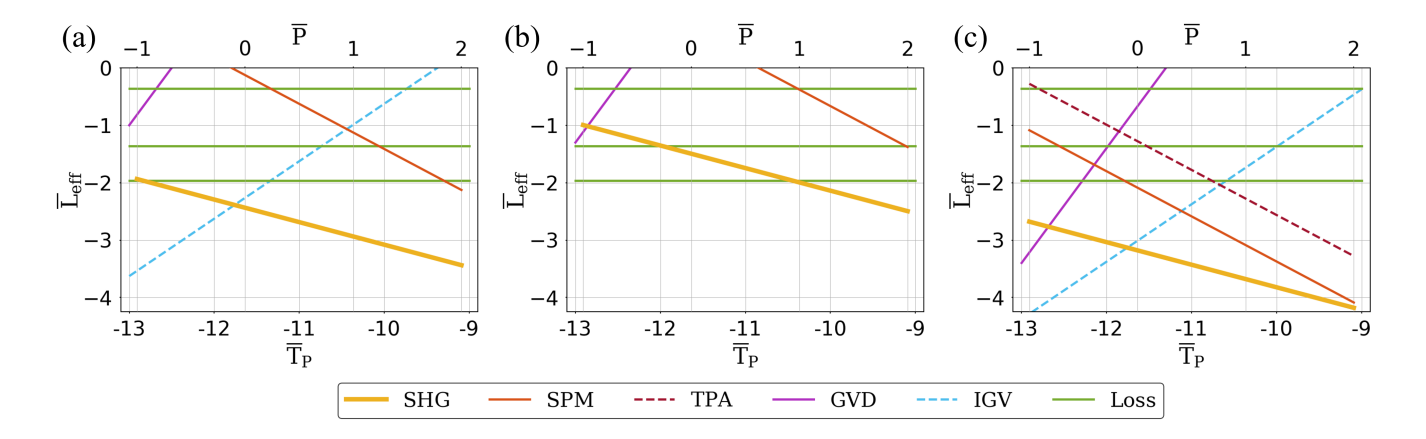


FIG. 2. Effective lengths for the 3 configurations under study: conf-LNX(a), conf-LNZ(b) and conf-AlG(c). See Table III for the definition of each effective length. Logarithm units are used for length $\bar{L}_{eff} = log_{10}(L_{eff}/1m)$, time $\bar{T}_p = log_{10}(T_p/1s)$, and power $\bar{P} = log_{10}(P/1W)$. Different effective lengths depend on either the power or pulse width, therefore a double x-axis is used to compare them. Specifically, \bar{L}_{SHG} (orange solid line), \bar{L}_{SPM} (red solid line) and \bar{L}_{TPA} (red dashed line) are a function of power (top x-axis \bar{P}), whereas \bar{L}_{GVD} (purple solid line) and \bar{L}_{IGV} (blue dashed line) are function of pulse width (bottom x-axis \bar{T}_p). Note that TPA is present in conf-AlG only. The effective lengths for losses of 0.1 dB/cm, 1 dB/cm and 4 dB/cm are independent of power and pulse width and are therefore represented by the 3 horizontal green lines, with increasing loss from bottom to top.

the waveguide where the maximum energy conversion is achieved.

III. ANALYSIS OF THE EFFECTIVE LENGTHS

The CE depends on the spatio-temporal dynamics described by Eqs. (1,2), which is the result of the interplay between several different physical effects. In this section, we introduce the definition of the effective length (L_{eff}) related to each of these effects. The comparison between the effective lengths provides an intuitive overview of the various achievable CE regimes and supports the numerical results discussed in the next section. It should be noted that we may define separate effective lengths at the FF and SH, respectively. On the other hand, since they have the same order of magnitude, for the sake of simplicity we refer to the effective lengths calculated at the FF. The full set of effective lengths are reported in Table III, alongside their dependence on the system parameters.

The effective length L_{IGV} related to the DIGV between FF and SH corresponds to the propagation length beyond which the input FF pulse and the generated SH pulse are temporally separated. The effective length related to the GVD is the well-known dispersion length L_{GVD} . L_{los} corresponds to the propagation length over which the power decays of a factor 1/e due to linear losses. In the following, we indicate with $L_{los}(0.1)$, $L_{los}(1)$ and $L_{los}(4)$ the effective lengths related to losses of 0.1 dB/cm, 1 dB/cm and 4 dB/cm, respectively. Similarly, L_{TPA} corresponds to the propagation length over which the power decays of a factor 1/e as a result of the TPA [45]. The effective length L_{SPM} indicates the

propagation length over which the Kerr-induced nonlinear phase accumulation due to SPM leads to a substantial shift of the phase-matching condition as well as to pulse distortion [46]. Similarly, we may define an effective length L_{XPM} for XPM, which is similar to L_{SPM} and therefore not included in the following analysis. Finally, L_{SHG} corresponds to the propagation length over which the power of FF drops to a fraction of 1/e as a result of the conversion of power via SHG to SH [45].

In order to facilitate a clear comparison between the different effective lengths, we introduce logarithmic units denoted as $\bar{L}_{eff} = \log 10 \, (L_{eff}/1\mathrm{m}), \ \bar{T}_p = \log 10 \, (T_P/1\mathrm{s}), \ \mathrm{and} \ \bar{P} = \log_{10} \, (P/1\mathrm{W}).$

Note that by definition, and as commonly accepted in the literature, the effective length for each physical effect introduced above is calculated with competing effects turned off. As such, calculating L_{SHG} implicitly assumes no pulse distortion or temporal walk-off (hence, a CW-like regime). Although this is an approximation,

Term	Length	Equation
DIGV	L_{IGV}	$T_p/\Delta eta_1$
GVD	L_{GVD}	T_p^2/eta_2
Loss	L_{los}	$1/\alpha$
TPA	L_{TPA}	$(e-1)/(\beta_{tpa}R_{ff}P)$
SPM	L_{SPM}	$1/(\Re\{\gamma_f\}R_{ff}P)$
SHG	L_{SHG}	$sech^{-1}(\sqrt{1/e})/(p\sqrt{P})$

TABLE III. Effective lengths and related equations

it is justified when SHG is the dominant process where its corresponding effective length is substantially shorter than the others, leading to large CE. As a rule of thumb, we expect high CE whenever L_{SHG} is 1 order of magnitude shorter than all the other effective lengths, that is, $\bar{L}_{SHG} < \bar{L}_x$ -1, where x={IGV, GVD, los, TPA, SPM}.

Let us consider Fig.2a, which reports the effective lengths for the case conf-LNX in Table I. We note that the conditions $\bar{L}_{SHG} < \bar{L}_{GVD} - 1$, $\bar{L}_{SHG} < \bar{L}_{SPM} - 1$, $\bar{L}_{SHG} < \bar{L}_{los0.1} - 1$ hold true for any value of P and T_p under consideration. This suggests that GVD and SPM do not affect significantly the SH conversion, and the same applies to weak linear losses of 0.1 dB/cm. On the other hand, the DIGV poses a lower limit to the pulse width: the condition $\bar{L}_{SHG} < \bar{L}_{IGV} - 1$ implies indeed $\bar{T}_p > -0.5\bar{P} - 10.8$. Similarly, high linear losses of 1 dB/cm and 4 dB/cm should be compensated by increasing the peak-power P: indeed $\bar{L}_{SHG} < \bar{L}_{los1} - 1$ and $\bar{L}_{SHG} < \bar{L}_{los4} - 1$ imply respectively $\bar{P} > -0.1$ and $\bar{P} > 1.2$.

A similar analysis can be done for the remaining configurations conf-LNZ and conf-AlG (see Fig.2(b,c) respectively). The main outcome is that, for each configuration, we identify the conditions on the pump power and pulse width that lead to high CE. In the next section, we discuss full numerical simulations of Eqs.(1,2), which confirms the qualitative conclusions drawn from the effective length analysis.

IV. CONVERSION EFFICIENCY PLOTS

In this section, we discuss the CE calculated via full simulation of Eqs. (1,2), and compare it with the analysis of the effective lengths introduced in the previous section.

Fig.3 displays the outcomes obtained for conf-LNX. The colormaps depict the results from numerical simulations for losses of 0.1 dB/cm (a), 1 dB/cm (b) and 4 dB/cm (c), respectively. Within each panel, the white dashed lines represent the boundaries of the conditions identified through the analysis of the effective lengths, namely $\bar{T}_p = -0.5\bar{P} - 10.8$ (diagonal line in a,b,c), $\bar{P} = -0.1$ (horizontal line in b), $\bar{P} = 1.2$ (horizontal line in c). The area enclosed by the white lines, denoted by a white star, identifies the region of the \bar{T}_p - \bar{P} plane where high CE is anticipated based on the effective lengths analvsis. Although qualitative in nature, this analysis captures, at almost zero computational cost, the range of pulse widths and peak powers leading to high CE. At the same time, it allows identifying the factors that hinder achieving high CE. For example, in this case, we note that DIGV impacts the CE, especially for short pulses, whereas cubic nonlinearities (SPM and XPM) have little to no impact.

To further assess the impact of DIGV and cubic nonlinearities, we have run separate simulations of Eqs. (1,2). This involved selectively disabling either the DIGV or SPM, XPM, as illustrated in Fig.4. Specifically, in Fig.4

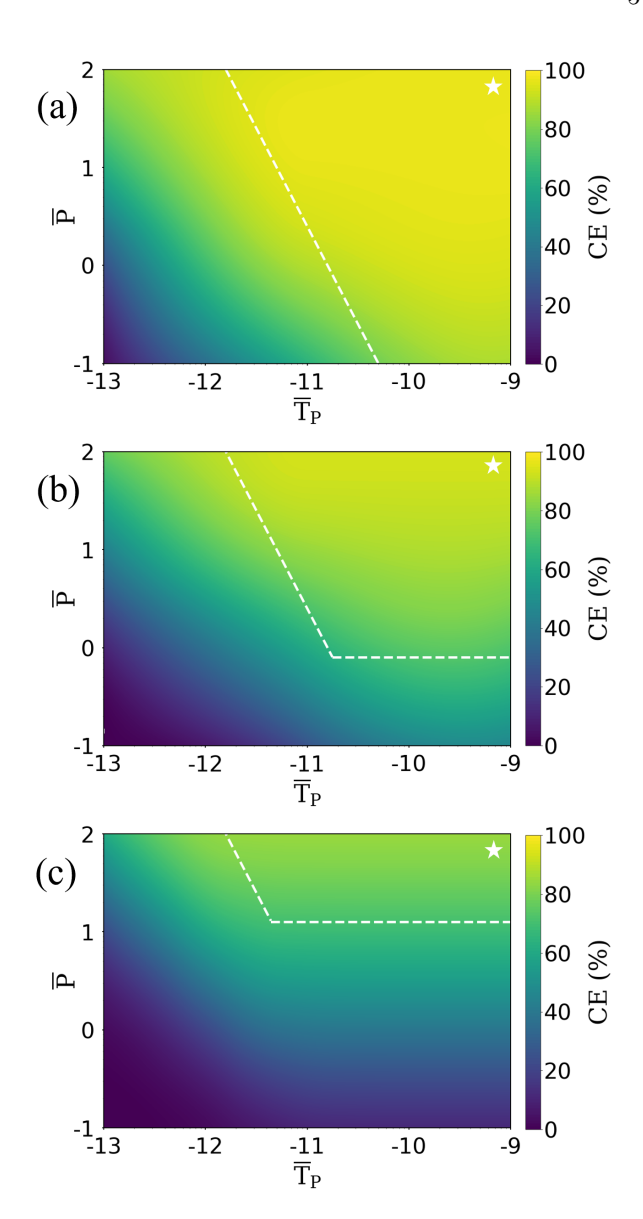


FIG. 3. Illustration of results for conf-LNX. The color maps display the CE computed from Eqs.(1,2) when linear losses are set respectively to 0.1 dB/cm (a), 1 dB/cm (b) and 4 dB/cm (c). Logarithm units are used for length $\bar{L}_{eff} = log_{10}(L_{eff}/1m)$, time $\bar{T}_p = log_{10}(T_p/1s)$, and power $\bar{P} = log_{10}(P/1W)$. The white dashed lines represent the boundaries of the conditions identified via the analysis of the effective lengths. In each panel, the white star (here on the top right) indicates the area enclosed by the white dashed lines where high CE is achieved according to the analysis of effective lengths.

we depict the variation in CE between the cases where all the terms of Eqs. (1,2) are taken into account and the case where DIGV is disabled (that is, $\Delta\beta_1$ is set to 0). Similarly, in Fig.4b we depict the variation in CE between the case where all the terms of Eqs. (1,2) are taken into account and the case where XPM and SPM are turned off (that is, $\gamma_{f,s}$ is set to 0).

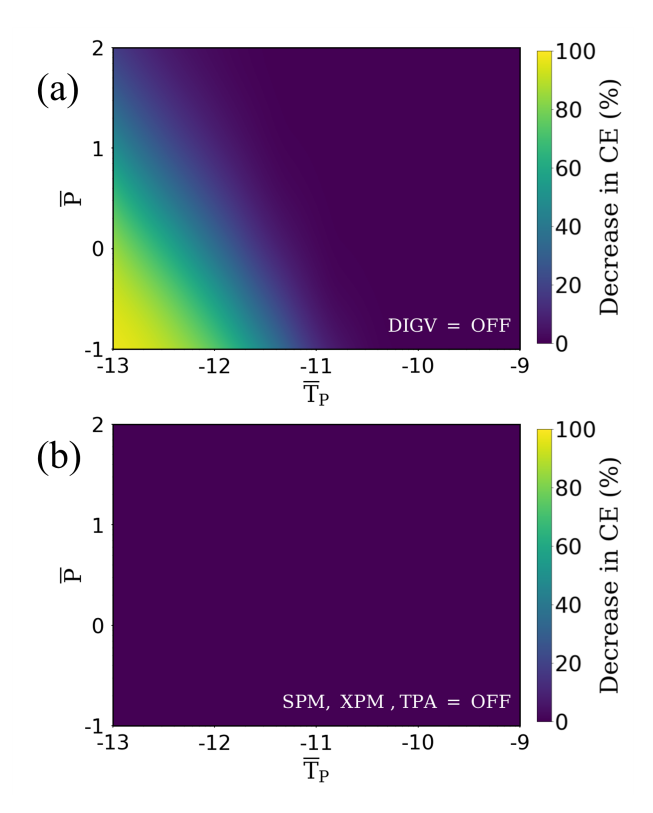


FIG. 4. (a): CE variation for conf-LNX when DIGV is disabled. (b): CE variation for conf-LNX when SPM and XPM are disabled. In both panels linear losses are 1 dB/cm.

The results in Fig.4 confirm that the DIGV is the main source of CE impairment in the sub-ps regime. Conversely, as anticipated SPM and XPM do not play any major role in the CE dynamics. Indeed, there is no significant CE variation in Fig.4b.

Similarly to Fig.3, Fig.5 reports the results for the case conf-LNZ of Table I. Once again, the analysis of the effective lengths (see Fig.2b) offers a qualitative overview of the different CE regimes. In particular, because \bar{L}_{SHG} is not significantly lower than \bar{L}_{los4} (the condition $\bar{L}_{SHG} < \bar{L}_{los4} - 1$ is not met), we expect that 4 dB/cm losses will suppress the SHG. This is confirmed by the numerical simulation of Eqs.(1,2), see Fig.5c. On the other hand, CE>80% can be achieved when losses are as low as 0.1 dB/cm, see Fig.5a. In addition, it is worth noting that because this configuration is characterized by null-DIGV, then the CE is independent of T_p .

The case conf-AlG illustrated in Fig.6 exhibits a more complex dynamics. The large nonlinear response of the AlGaAs, along with the strong modal confinement fostered by the large core-to-cladding refractive index difference, leads to substantial SH conversion over a mm long scale even for peak power levels as low as hundreds mW (see \bar{L}_{SHG} in Fig.2c). However, cubic nonlinear effects (SPM, XPM, TPA) are dramatically enhanced at the same time, which strongly impacts the CE. Indeed, differently from the previous cases conf-LNX

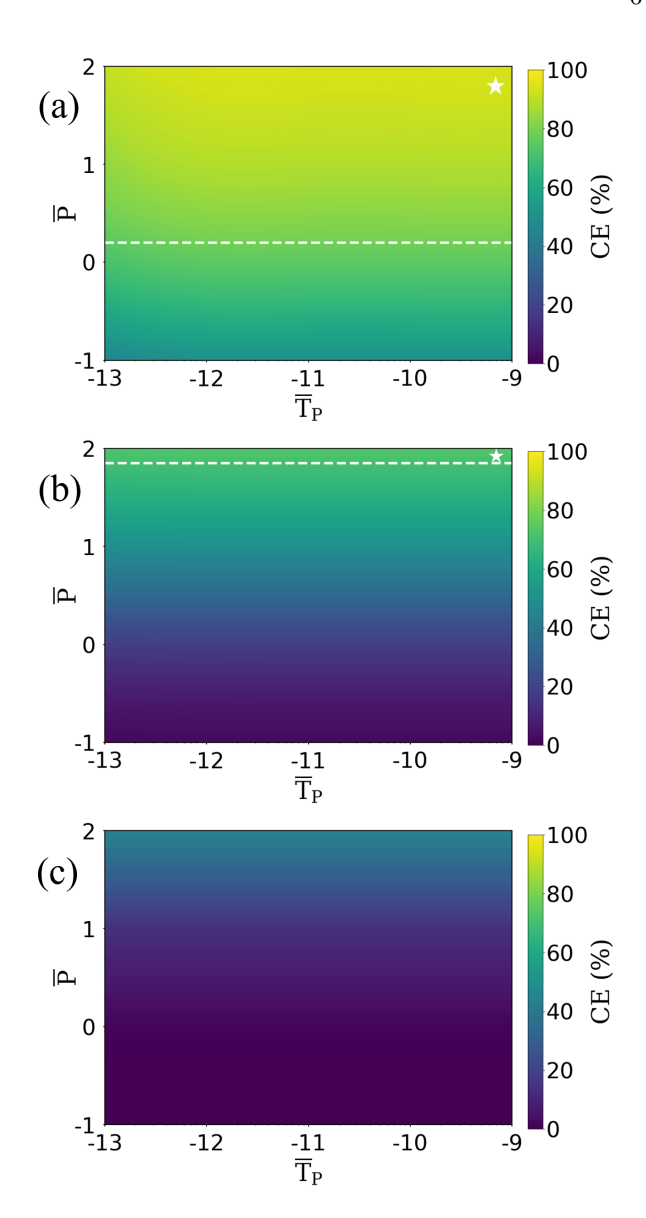


FIG. 5. Same as Fig.3, but for the case conf-LNZ.

and conf-LNZ, we observe from Fig.2c that the condition $\bar{L}_{SHG} < \bar{L}_{SPM,TPA} - 1$ requires $\bar{P} < 0.3$ (i.e. P< 2 W). This suggests that cubic nonlinearities are the major source of CE impairment when the peak power exceeds a few Watts. This scenario is confirmed by the simulations of Eqs.(1,2). Indeed, for all the values of linear losses considered in this work, we observe a decrease of CE when P > 5 W.

The simulation of Eqs.(1,2) with SPM, XPM and TPA turned off, reported in Fig.7b, confirms this trend.

The dynamics related to DIGV and linear losses are instead similar to those observed in conf-LNX: high linear losses set a lower limit to P, whereas the DIGV impairs significantly the CE in the sub-ps regime, as displayed in Fig. 7a.

Overall, from the results in Figs. (3-7), we can draw out

a general CE trend for different power and pulse width regimes. We observe that in the case of conf-LNX, high CE> 80% is achieved when losses are ≤ 1 dB/cm, for peak power exceeding ~ 30 W and pulse width exceeding ~ 5 ps. The corresponding waveguide length (indicated as z_{max} in Section 2) is 4mm or shorter. Similar CE and lengths are found for conf-AlG but for substantially lower peak power (~ 2 W). Conversely, high-power operation jeopardises the CE due to cubic nonlinearities.

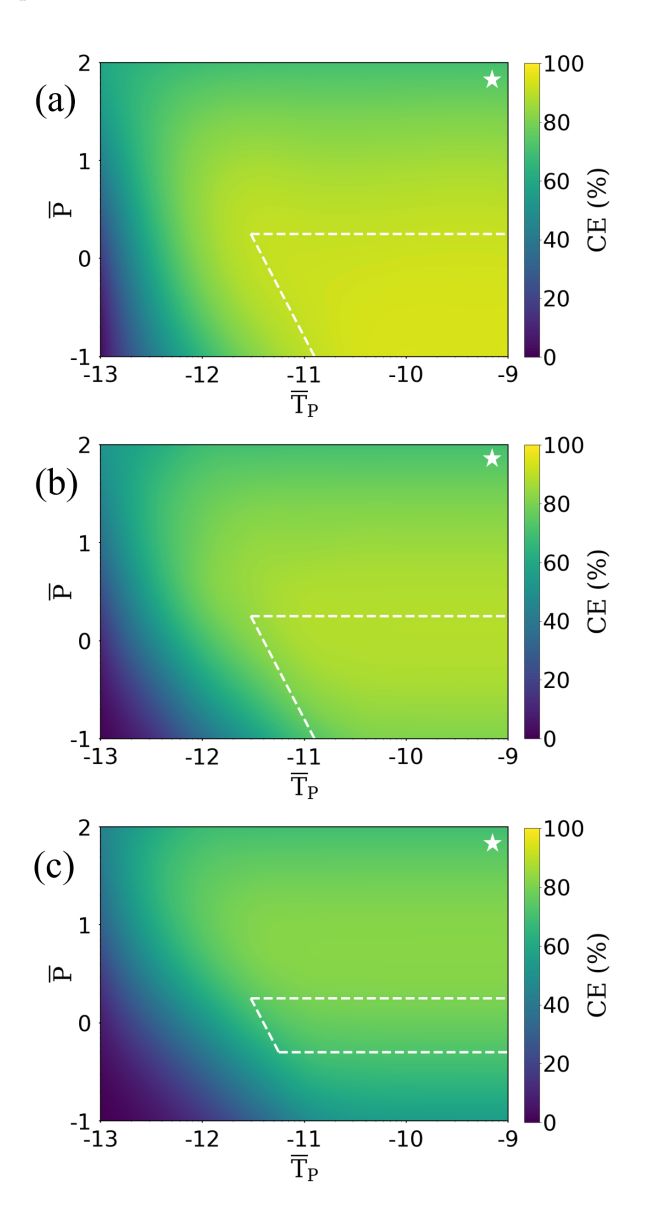


FIG. 6. Same as Fig.3, but for the case conf-AlG.

In the sub-ps pulse regime, neither conf-LNX or conf-AlG can achieve large CE, mainly as a result of the DIGV between FF and SH. In contrast, thanks to the null-DIGV condition, conf-LNZ allows achieving high CE> 80% in the sub-ps regime when losses are 0.1 dB/cm or smaller, again for pump peak power exceeding ~ 30 W. Interestingly enough, this configuration also

exhibits adequate CE \sim 50% in the sub-ps, sub-W regime when losses are 0.1 dB/cm or smaller.

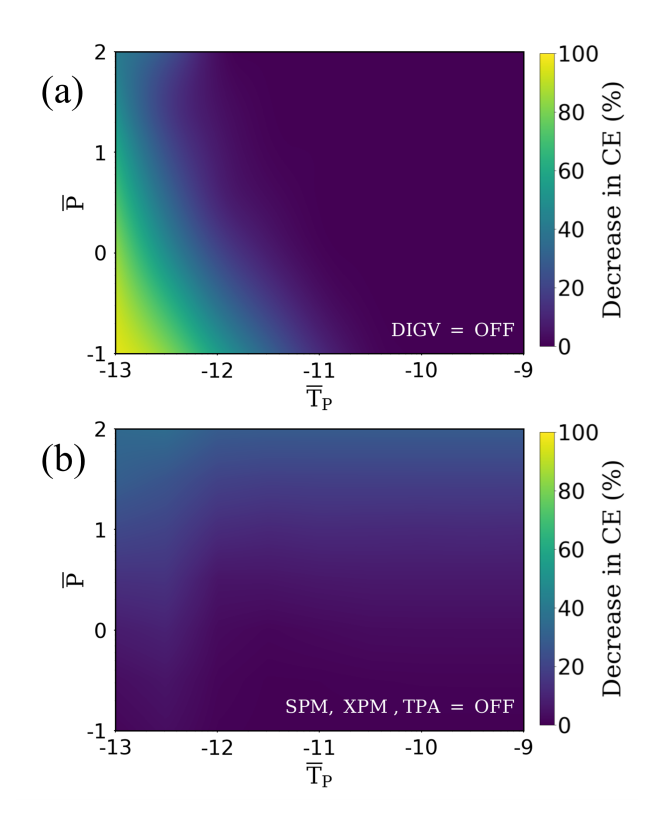


FIG. 7. (a): CE variation for conf-AlG when DIGV is disabled. (b): CE variation for conf-AlG when SPM, XPM and TPA are disabled. In both panels linear losses are 1 dB/cm.

Overall, from the results in Figs.(3-7), we can draw out a general CE trend for different power and pulse width regimes. We observe that in the case of conf-LNX, high CE> 80% is achieved when losses are ≤ 1 dB/cm, for peak power exceeding ~ 30 W and pulse width exceeding ~ 5 ps. The corresponding waveguide length (indicated as z_{max} in Section 2) is 4mm or shorter.

Similar CE and lengths are found for conf-AlG but for substantially lower peak power (\sim 2 W). Conversely, high-power operation jeopardises the CE due to cubic nonlinearities.

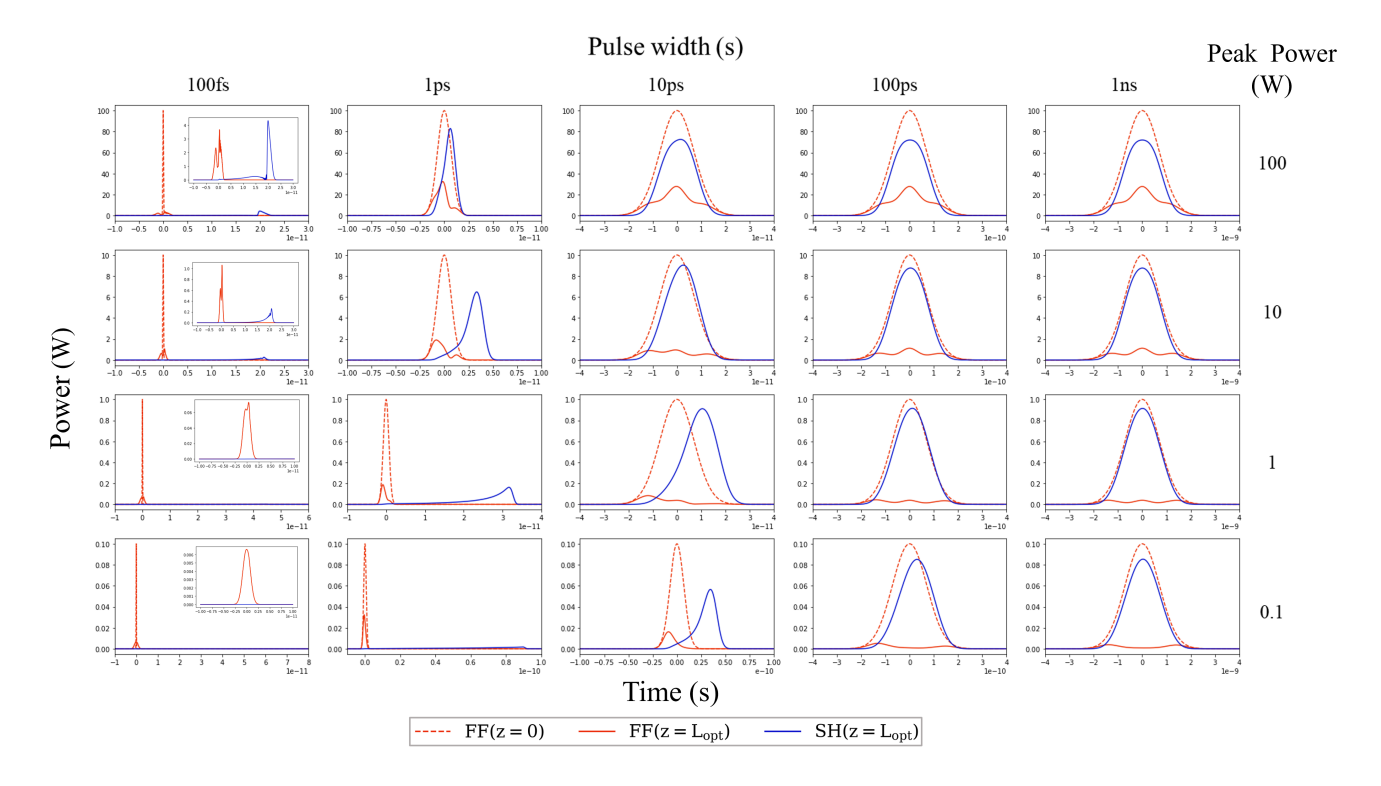


FIG. 8. Input FF (red dashed line), output SH (blue solid line) and output FF (red solid line) pulses at maximum CE for conf-AlG when losses are 1 dB/cm (see Fig.6b for corresponding CE values) for different values of input FF peak power (0.1 W to 100 W from bottom to top) and input FF pulse width (100fs to 1ns from left to right).

V. TEMPORAL AND SPECTRAL PROFILES

In this section, we illustrate the temporal and spectral profiles for different regimes of power and pulse width. We refer to the case of conf-AlG, but similar dynamics are observed for conf-LNX. Fig.8 illustrates the FF and SH pulses calculated at the optimal length for maximum CE. For pulses longer than 100 ps, the generated SH shows a Gaussian profile, identical to the input FF pulse, regardless of the power level. This is due to the limited walk-off between FF and SH, which leads to SHG dynamics occurring in a CW-like regime. For conf-LNZ we see no walk-off and therefore only preserved Gaussian shapes for SH at all pulse widths investigated.

As the pulse width is reduced to 10ps or less, we observe the generation of an asymmetric SH pulse with an extended tail, a clear signature of the walk-off between FF and SH. This tail is more pronounced at lower power levels, where a longer propagation length is required to achieve maximum CE, leading to an increased walk-off.

In the high-power, ultra-short pulse regime (100 fs or less), in addition to the tail, we also observe SH pulse fragmentation, caused by a non-trivial combination of SPM, XPM and walk-off effects. Regarding the FF pulse, it exhibits strong symmetric reshaping dominated by SPM for longer pulses (>100 ps), with additional tailing and fragmentation for shorter pulses. The fragmentation effect increases dramatically with power, leading to the

generation of a comb of spikes, as shown in Fig.9(c,d), where significant spectral distortion is also evident.

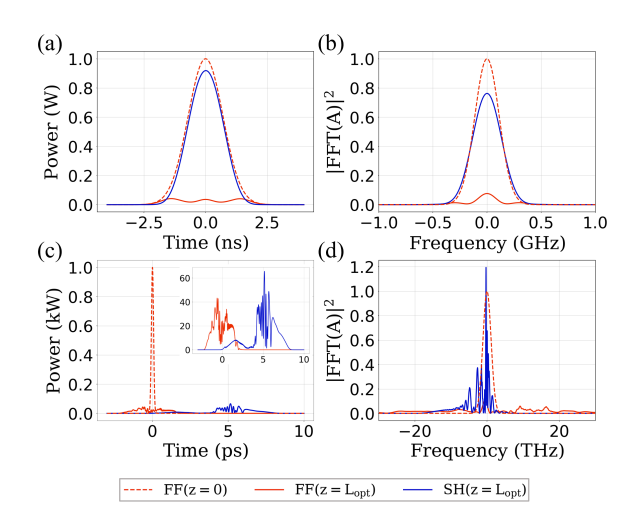


FIG. 9. Illustration of fragmentation effect and reduced efficiency at high powers with short pulses. Pulse shape and related spectra for conf-AlG with P=1W with T_0 =1ns in (a,b) and P=1kW with T_0 =100fs in (c,d). Pulse shapes taken at L_{opt} where CE is the maximum for each case. Loss is set to 1dB/cm.

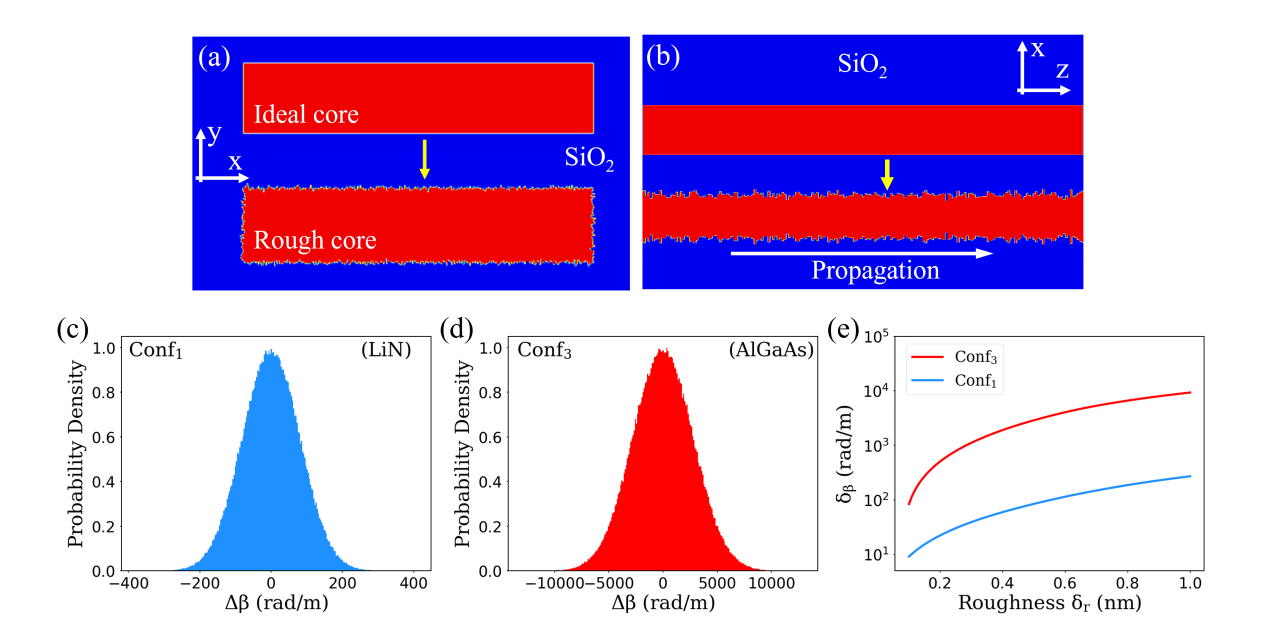


FIG. 10. a) Illustration of the simulated cross-section with random roughness. Top: unperturbed rectangular cross-section on the xy transverse plane without roughness; bottom: cross-section with added roughness. (b): Illustration of simulated roughness along the propagation direction. Top: unperturbed waveguide; bottom: waveguide with added roughness. (c,d): An example of the probability distribution function of the phase mismatch $\Delta\beta$ used in our simulations. Here roughness has a standard deviation $\delta_r = 0.4$ nm. e): standard deviation δ_β of the phase-mismatch versus standard deviation of roughness δ_r for conf-LNX and conf-AlG.

VI. ROBUSTNESS AND WAVELENGTH TUNABILITY

Due to fabrication errors, the actual dimensions of the waveguides under analysis could deviate from the designed values, resulting in a phase-mismatch that typically degrades the CE.

As it is illustrated in Fig.11, a shift of the FF typically allows compensating for the phase-mismatch. For example, a ± 10 nm variation in the width of the LiN waveguide of conf-LNX, corresponding to a realistic fabrication error, could be compensated by a variation of \pm 20 nm (in wavelength) of the FF.

From another perspective, Fig.11 also suggests that the FF could be tuned over a wide spectral region by setting opportunely the waveguide dimensions. Interestingly enough, the LiN and AlGaAs platforms exhibit an opposite trend. While the phase-matching in the AlGaAs waveguide is almost insensitive to width variations, and the height is then used to tune the FF, the opposite occurs in the LiN waveguides.

On the other hand, it should be noted that while the phase-matching condition can be achieved as illustrated in Fig.11, however a variation in the waveguide dimensions and/or in the FF will modify the coefficients of Eqs.(1,2), which ultimately determines the CE. Variations of a few nanometers in the waveguide dimensions or in the FF wavelength do not affect significantly the overall CE dynamics in the case of conf-LNX and conf-

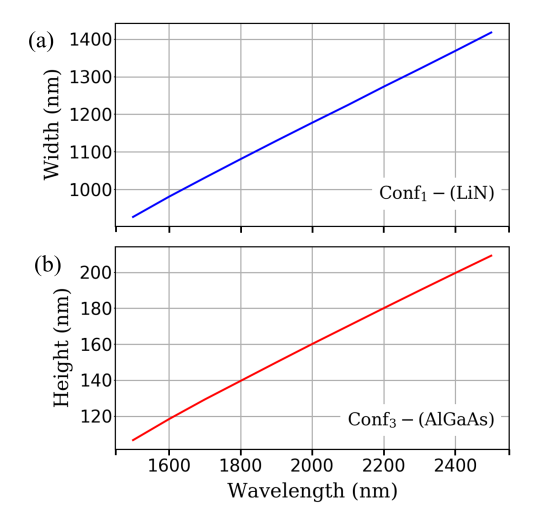


FIG. 11. Tuning of the phase-matching condition. (a) Width-FF wavelength relation to preserve phase-matching in a LNOI waveguide with fixed height $h=470\mathrm{nm}$. For width $w=960\mathrm{nm}$ we have the waveguide of conf-LNX in Table I (FF wavelength=1550 nm). (b) Height-FF wavelength relation to preserving phase-matching in an AlGaAsOI waveguide with fixed width $h=575\mathrm{nm}$. For height $h=111\mathrm{nm}$ we have the waveguide of conf-AlG in Table I (FF wavelength=1550 nm).

AlG. On the contrary, in the case of conf-LNZ, these variations hinder the zero-DIGV condition, resulting in a substantial drop of CE for short pulses $(T_p < 0.1 \text{ns})$.

Along with fabrication errors, surface roughness could be a further source of CE impairment. In addition to contributing to linear losses (whose overall value is indicated by $\alpha_{f,s}$ in Eqs.(1,2)), roughness corresponds to a random variation of the cross-section of the waveguide, as illustrated in Fig.10(a,b). This variation induces in turn a random phase-mismatch along the propagation direction z. To investigate the influence of roughness, we have created cross-section profiles with random roughness having Gaussian statistical distribution with 0 average and standard deviation δ_r . Each cross-section profile corresponds to a phase-mismatch $\Delta\beta$, computed with Comsol Multiphysics, which exhibits a Gaussian-like distribution as illustrated in Fig. 10(c,d). We have then simulated Eqs.(1,2) assuming a variable phase-mismatch $\Delta\beta(z)$ along the propagation direction and with the appropriate statistical distribution (see in Fig.10e the relation among roughness and standard deviation of $\Delta \beta(z)$).

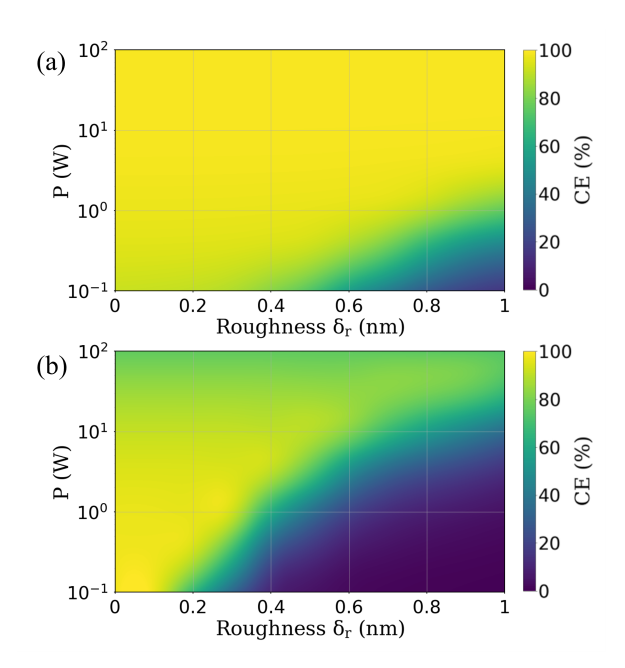


FIG. 12. CE as a function of the peak power \bar{P} (logarithm units) and roughness size (deviation δ_r). Panel (a) and (b) refer respectively to conf-LNX and conf-AlG, for pulse width $T_p = 1$ ns and losses of 0.1 dB/cm.

The results of the simulations are illustrated in Fig.12 for pulses of 1 ns width and losses of 0.1 dB/cm. The CE is computed as a function of the roughness standard deviation δ_r and the peak power \bar{P} for the LNOI waveguide of conf-LNX and the AlGaAsOI waveguide of conf-AlG (panels a and b, respectively). While the LiN waveguide of conf-LNX is weakly affected by roughness for peak power levels P exceeding 1 W (see Fig.12a), the AlGaAs waveguide of conf-AlG is less robust and the CE is strongly affected when $\delta_r > 0.4$ nm (see Fig.12b). This is essentially due to the fact that a smaller waveguide undergoes a higher relative variation of its dimensions for the same δ_r .

VII. CONCLUSION

The last decade has been characterised by a rising interest towards LNOI and AlGaAsOI platforms. The high refractive index contrast with respect to the cladding represents a crucial factor for the miniaturization of photonic devices on chip, including those for wavelength conversion, which is one of the most important operations in the nonlinear domain. However, it is not yet clear which conversion efficiency can be obtained in these platforms, and whether and within what regimes of power and pulse width they can exceed the traditional counterparts used for nonlinear conversion, especially PPLN and AlGaAs/GaAs waveguides.

In this work, we compared the two platforms in terms of compactness and SHG conversion efficiency, outlining the foreseeable performance for different regimes of pulse duration and power. Note that the validity of our findings is contingent upon the absence of damage to the waveguides at higher powers. Damage thresholds are difficult to be evaluated given the scarcity of data available [40, 47–50] and their dependence on the quality of the fabrication process.

For each platform, we identified an optimal configuration (conf-LNX, conf-AlG) that maximises the quadratic nonlinear coefficients, therefore minimising the overall footprint. In addition, we have found a further configuration (conf-LNZ) for LiNOI characterized by zero DIGV between the phase-matched modes, which preserves their temporal overlap in propagation. Our analysis suggests that overall, both LNOI and AlGaAsOI may lead to very high nonlinear conversion, comparable if not superior to standard LiN diffused PPLN and AlGaAs/GaAs waveguides, but with an unprecedented small footprint. For this purpose, Table IV reports a comparison against recent works based either on standard PPLN and AlGaAs/GaAs waveguides, as well as AlGaAsOI and LNOI waveguides.

Nevertheless, our findings indicate some key differences between these 2 platforms. Indeed, we envisage that AlGaAsOI will be the reference platform for low peak power operation (not exceeding a few Watts) and relatively long pulses, from 10 ps-wide up to CW. The large core to cladding index difference guarantees strongly confined modes with sub-um² modal area, which may provide CE exceeding 80% when losses are ≤ 1 dB/cm (see Fig.6a,b). These estimates represent extremely high conversion values, which are even more relevant when taking into account the reduced length of the waveguide (few mm) and a total footprint of just $\sim 1000~\rm um^2$, 3 orders of magnitude smaller than traditional waveguides offering a similar performance (see [14] in Table IV).

Ref	Technology	Geometry	Performance
[14]	Zinc indiffused LiN PPLN	Rib waveguide, dim= $13\mu m \times 50\mu m$, 4 cm long	CE=74% with 3.37W CW pump,loss=0.12 dB/cm (FF)
[15]	AlGaAs/GaAs	Bragg reflection ridge waveguide dim= $4\mu m \times 4.4\mu m$, 2.17 mm long	CE=2% with 1.8 ps pulsed pump, 20 W peak power, loss=8.7 dB/cm (FF)
[18]	LNOI PPLN (null-DIGV)	ridge waveguide, dim=2 $\mu m \times 0.7 \mu m$, 6 mm long	CE>50% with 50fs pulsed pump, 1.6W peak power, loss=0.1 dB/cm(FF)
[20]	LNOI PPLN	ridge waveguide, dim=1.4 μ m × 0.6 μ m, 4 mm long	CE=53% with 0.25W CW pump, loss $$<\!2.5\mathrm{dB/cm(FF)}$$
[21]	AlGaAsOI	dim= $740nm \times 100nm$, 2.7 mm long	CE \sim 0.8% with 100fs pulsed pump,12.5W peak power, loss=13 dB/cm (FF)
This Work	LNOI	conf-LNX (dim=960nm \times 470nm), \sim 4 mm long (for 30W peak power)	CE> 80% with >5 ps pulsed pump,>30 W peak power, loss ≤ $1dB/cm$
This Work	LNOI (null-DIGV)	conf-LNZ (dim=3945 $nm \times 1162nm$), ~ 1 cm long (for 30W peak power)	CE> 80% with >100 fs pulsed pump,>30 W peak power, loss $\leq 0.1 dB/cm$
This Work	AlGaAsOI	conf-AlG (dim=575nm × 111nm), ~ 1 mm long (for 3 W power)	CE> 80% with >10 ps pulsed pump,<3 W peak power, loss $\leq 1dB/cm$

TABLE IV. Comparison between state-of-the-art works and results predicted in this work. All data, if not explicitly mentioned in the corresponding manuscript, are otherwise inferred by the information provided in [14, 15, 18, 20, 21]. The notation null-DIGV indicates that the FF and SH modes are characterized by null-DIGV (or quasi-null-DIGV).

However, we foresee two main issues. First, it remains to be seen whether these loss values will be feasible in the future in a waveguide with a transverse size as small as the one of conf-AlG. The current losses reported in the literature for AlGaAsOI waveguides of a similar size are much higher (13 dB/cm at the FF, see [21] in Table IV), which impairs substantially the CE. Second, our analysis suggests that the small transverse size brings another issue, namely, surface roughness may dramatically impair (if not completely annihilate) the CE. On the other hand, both losses and detrimental roughness effects will likely be substantially reduced in the future with the improvement of manufacturing processes.

We envisage that LNOI waveguides will be instead the reference platform for high peak power operation exceeding a few tens of Watts. Besides being TPA-free, the lower core-to-cladding index difference (compared to AlGaAsOI) results in a larger mode area and a larger transverse dimension of the waveguide. This ultimately minimises the unwanted cubic nonlinearities, which affect instead the AlGaAsOI platform when the pump peak power exceeds a few Watts. For the same reasons, the LNOI platform seems largely unaffected by the phase-mismatch induced by surface roughness. As a result, values of CE> 80% could be achieved when losses are $\leq 1~\mathrm{dB/cm}$ in conf-LNX, provided that the pulse width is long enough, a few ps at least. Moreover, the sub-ps regime can be achieved when the zero-DIGV condition is fulfilled between the phase-matched modes at the FF and SH, which is the case of conf-LNZ when losses are as low as 0.1 dB/cm.

It is worth noting that such low-loss values are already feasible in the LNOI platform. For comparison, recent experiments have demonstrated CE \sim 50% in the sub-ps pulse regime and 1.6 W pump peak power (see [18] in Table IV) in a 6mm long LNOI waveguide characterized by losses of \sim 0.1 dB/cm and by almost null-DIGV between FF and SH modes, which is similar to the results obtained in our simulation of conf-LNZ for similar levels of peak power, losses and pulse duration.

As reported in Section 5, while our simulations have focused on SHG with FF wavelength of 1550nm, how-

ever, the phase-matching condition can be adjusted via the geometric parameters, which indicates both a wide wavelength tunability of the SHG, as well as a partial robustness against manufacturing errors. Although timeconsuming, full-scale numerical simulations should be run for each specific FF value, however, it is worth noting that the effective lengths analysis introduced in Section 3 provides an extremely fast and efficient tool to qualitatively estimate the different CE regimes as a function of the system parameters.

- L. Ottaviano, M. Pu, E. Semenova, and K. Yvind, Low-loss high-confinement waveguides and microring resonators in AlGaAs-on-insulator, Optics Letters 41, 3996 (2016).
- [2] F. Baboux, G. Moody, and S. Ducci, Nonlinear integrated quantum photonics with algaas, Optica 10, 917 (2023).
- [3] J. Lin, F. Bo, Y. Cheng, and J. Xu, Advances in on-chip photonic devices based on lithium niobate on insulator, Photonics Research 8, 1910 (2020).
- [4] A. Boes, B. Corcoran, L. Chang, J. Bowers, and A. Mitchell, Status and potential of lithium niobate on insulator (lnoi) for photonic integrated circuits, Laser & Photonics Reviews 12, 1700256 (2018).
- [5] S. Kuma, Y. Miyamoto, K. Tsutsumi, N. Sasao, and S. Uetake, 4.8 μ m difference-frequency generation using a waveguide-ppln crystal and its application to midinfrared lamb-dip spectroscopy, Optics Letters **38**, 2825 (2013).
- [6] K.-D. F. Büchter, H. Herrmann, C. Langrock, M. M. Fejer, and W. Sohler, All-optical Ti:PPLN wavelength conversion modules for free-space optical transmission links in the mid-infrared, Opt. Lett. 34, 470 (2009).
- [7] Y. L. Lee, B.-A. Yu, C. Jung, Y.-C. Noh, J. Lee, and D.-K. Ko, All-optical wavelength conversion and tuning by the cascaded sum-and difference frequency generation (csfg/dfg) in a temperature gradient controlled ti: Ppln channel waveguide, Optics Express 13, 2988 (2005).
- [8] H. Ishikawa and T. Kondo, Birefringent phase matching in thin rectangular high-index-contrast waveguides, Applied Physics Express 2, 042202 (2009).
- [9] S. Ducci, L. Lanco, V. Berger, A. De Rossi, V. Ortiz, and M. Calligaro, Continuous-wave second-harmonic generation in modal phase matched semiconductor waveguides, Applied physics letters 84, 2974 (2004).
- [10] M. Yamada, N. Nada, M. Saitoh, and K. Watanabe, First-order quasi-phase matched linbo3 waveguide periodically poled by applying an external field for efficient blue second-harmonic generation, Applied Physics Letters 62, 435 (1993).
- [11] T. Kishimoto, K. Inafune, Y. Ogawa, H. Sasaki, and H. Murai, Highly efficient phase-sensitive parametric gain in periodically poled LiNbO3 ridge waveguide, Opt. Lett. 41, 1905 (2016).
- [12] K. Moutzouris, S. Venugopal Rao, M. Ebrahimzadeh, A. De Rossi, M. Calligaro, V. Ortiz, and V. Berger, Second-harmonic generation through optimized modal phase matching in semiconductor waveguides, Applied physics letters 83, 620 (2003).
- [13] D. F. Logan, M. Giguere, A. Villeneuve, and A. S. Helmy, Widely tunable mid-infrared generation via frequency conversion in semiconductor waveguides, Opt. Lett. 38, 4457 (2013).
- [14] L. G. Carpenter, S. A. Berry, A. C. Gray, J. C. Gates, P. G. Smith, and C. B. Gawith, Cw demonstration of shg

- spectral narrowing in a ppln waveguide generating 2.5 w at 780 nm, Optics Express 28, 21382 (2020).
- [15] P. Abolghasem, J. Han, B. J. Bijlani, A. Arjmand, and A. S. Helmy, Highly efficient second-harmonic generation in monolithic matching layer enhanced al _x ga _{1-x} as bragg reflection waveguides, IEEE Photonics Technology Letters 21, 1462 (2009).
- [16] M. Savanier, A. Andronico, A. Lemaître, E. Galopin, C. Manquest, I. Favero, S. Ducci, and G. Leo, Large second-harmonic generation at 1.55 μmin oxidized algaas waveguides, Optics letters 36, 2955 (2011).
- [17] R. Luo, Y. He, H. Liang, M. Li, and Q. Lin, Highly tunable efficient second-harmonic generation in a lithium niobate nanophotonic waveguide, Optica 5, 1006 (2018).
- [18] M. Jankowski, C. Langrock, B. Desiatov, A. Marandi, C. Wang, M. Zhang, C. R. Phillips, M. Lončar, and M. Fejer, Ultrabroadband nonlinear optics in nanophotonic periodically poled lithium niobate waveguides, Optica 7, 40 (2020).
- [19] S. Saravi, T. Pertsch, and F. Setzpfandt, Lithium niobate on insulator: An emerging platform for integrated quantum photonics, Advanced Optical Materials 9, 2100789 (2021).
- [20] C. Wang, C. Langrock, A. Marandi, M. Jankowski, M. Zhang, B. Desiatov, M. M. Fejer, and M. Lončar, Ultrahigh-efficiency wavelength conversion in nanophotonic periodically poled lithium niobate waveguides, Optica 5, 1438 (2018).
- [21] S. May, M. Kues, M. Clerici, and M. Sorel, Second-harmonic generation in AlGaAs-on-insulator waveguides, Optics Letters 44, 1339 (2019).
- [22] S. May, M. Clerici, and M. Sorel, Supercontinuum generation in dispersion engineered AlGaAs-on-insulator waveguides, Scientific Reports 11, 2052 (2021).
- [23] M. L. Madsen, E. Z. Ulsig, S. Folsach, P. H. Godoy, E. J. Stanton, and N. Volet, Mid-infrared difference-frequency generation in algaas-on-insulator waveguides, JOSA B 40, 1742 (2023).
- [24] J. Haines, M. Gandolfi, Y. Franz, C. De Angelis, and M. Guasoni, Mid-infrared frequency generation via intermodal difference frequency generation in AlGaAs-oninsulator waveguides, Frontiers in Photonics 2, 788174 (2021).
- [25] T. H. Stievater, R. Mahon, D. Park, W. S. Rabinovich, M. W. Pruessner, J. B. Khurgin, and C. J. K. Richardson, Mid-infrared difference-frequency generation in suspended GaAs waveguides, Opt. Lett. 39, 945 (2014).
- [26] L. Carletti, A. Locatelli, O. Stepanenko, G. Leo, and C. De Angelis, Enhanced second-harmonic generation from magnetic resonance in AlGaAs nanoantennas, Optics Express 23, 26544 (2015).
- [27] M. Gandolfi, L. Carletti, A. Tognazzi, A. C. Cino, C. De Angelis, and M. Guasoni, Near to short wave infrared light generation through AlGaAs-on-insulator

- nanoantennas, Optics Express 31, 31051 (2023).
- [28] M. Pu, L. Ottaviano, E. Semenova, and K. Yvind, Efficient frequency comb generation in algaas-on-insulator, Optica 3, 823 (2016).
- [29] M. Kolesik and J. V. Moloney, Nonlinear optical pulse propagation simulation: From Maxwell's to unidirectional equations, Phys. Rev. E 70, 036604 (2004).
- [30] Z. Huang, C. Tu, S. Zhang, Y. Li, F. Lu, Y. Fan, and E. Li, Femtosecond second-harmonic generation in periodically poled lithium niobate waveguides written by femtosecond laser pulses, Optics letters 35, 877 (2010).
- [31] A. C. Peacock, P. Mehta, P. Horak, and N. Healy, Nonlinear pulse dynamics in multimode silicon core optical fibers, Optics Letters 37, 3351 (2012).
- [32] R. Klein, G. Kugel, A. Maillard, K. Polgár, and A. Péter, Absolute non-linear optical coefficients of linbo3 for near stoichiometric crystal compositions, Optical Materials 22, 171 (2003), proceedings of the Scientific Committe of the French Research Group "GDR 1148 CNRS": LAS-MAT: Research Group on Laser Materials.
- [33] W. J. Alford and A. V. Smith, Wavelength variation of the second-order nonlinear coefficients of knbo3, ktiopo4, ktioaso4, linbo3, liio3, β-bab2o4, kh2po4, and lib3o5 crystals: a test of miller wavelength scaling, J. Opt. Soc. Am. B 18, 524 (2001).
- [34] R. Schiek and T. Pertsch, Absolute measurement of the quadratic nonlinear susceptibility of lithium niobate in waveguides, Opt. Mater. Express 2, 126 (2012).
- [35] I. Shoji, T. Kondo, A. Kitamoto, M. Shirane, and R. Ito, Absolute scale of second-order nonlinear-optical coefficients, J. Opt. Soc. Am. B 14, 2268 (1997).
- [36] M. Ohashi, T. Kondo, R. Ito, S. Fukatsu, Y. Shiraki, K. Kumata, and S. Kano, Determination of quadratic nonlinear optical coefficient of Al_xGa_{1-x}As system by the method of reflected second harmonics, Journal of applied physics 74, 596 (1993).
- [37] Z. Yang, P. Chak, A. D. Bristow, H. M. van Driel, R. Iyer, J. S. Aitchison, A. L. Smirl, and J. E. Sipe, Enhanced second-harmonic generation in AlGaAs microring resonators, Opt. Lett. 32, 826 (2007).
- [38] R. DeSalvo, A. Said, D. Hagan, E. Van Stryland, and M. Sheik-Bahae, Infrared to ultraviolet measurements of two-photon absorption and n/sub 2/ in wide bandgap solids, IEEE Journal of Quantum Electronics 32, 1324 (1996).
- [39] I. A. Kulagin, R. A. Ganeev, R. I. Tugushev, A. I. Ryas-

- nyansky, and T. Usmanov, Components of the third-order nonlinear susceptibility tensors in kdp, dkdp and linbo3 nonlinear optical crystals, Quantum Electronics **34**, 657 (2004).
- [40] D. Nikogosyan, Nonlinear Optical Crystals: A Complete Survey, Nonlinear Optical Crystals: A Complete Survey: , ISBN 978-0-387-22022-2. Springer Science+Business Media, Inc., 2005, 428 (2005).
- [41] O. Beyer, D. Maxein, K. Buse, B. Sturman, H. Hsieh, and D. Psaltis, Femtosecond time-resolved absorption processes in lithium niobate crystals, Optics letters 30, 1366 (2005).
- [42] S. Gehrsitz, F. K. Reinhart, C. Gourgon, N. Herres, A. Vonlanthen, and H. Sigg, The refractive index of AlxGa1-xAs below the band gap: Accurate determination and empirical modeling, Journal of Applied Physics 87, 7825 (2000).
- [43] I. H. Malitson, Interspecimen comparison of the refractive index of fused silica, Josa 55, 1205 (1965).
- [44] D. E. Zelmon, D. L. Small, and D. Jundt, Infrared corrected sellmeier coefficients for congruently grown lithium niobate and 5 mol.% magnesium oxide-doped lithium niobate, JOSA B 14, 3319 (1997).
- [45] R. W. Boyd, Nonlinear Optics, Third Edition, 3rd ed. (Academic Press, Inc., USA, 2008).
- [46] G. Agrawal, Nonlinear Fiber Optics., Vol. 5th (Academic Press, 2013).
- [47] A. Garg, A. Kapoor, and K. Tripathi, Laser-induced damage studies in GaAs, Optics & Laser Technology 35, 21 (2003).
- [48] H. Qi, Q. Wang, X. Zhang, Z. Liu, S. Zhang, J. Chang, W. Xia, and G. Jin, Theoretical and experimental study of laser induced damage on gaas by nanosecond pulsed irradiation, Optics and Lasers in Engineering 49, 285 (2011).
- [49] Y. Furukawa, A. Yokotani, T. Sasaki, H. Yoshida, Yoshida, F. Nitanda, and M.Sato, vestigation of bulk laser damage threshold lithium niobate single crystals by Q-switched ofApplied Physics pulse laser, Journal 3372 (1991),https://pubs.aip.org/aip/jap/articlepdf/69/5/3372/18639983/3372_1_online.pdf.
- [50] S. Kato, S. Kurimura, H. H. Lim, and N. Mio, Induced heating by nonlinear absorption in linbo3-type crystals under continuous-wave laser irradiation, Optical Materials 40, 10 (2015).